

Magnetically-Driven Accretion-Disk Winds and Ultra-Fast Outflows in PG 1211+143

KEIGO FUKUMURA^{1,2}, FRANCESCO TOMBESI^{3,4}, DEMOSTHENES KAZANAS³, CHRIS SHRADER^{3,5}, EHUD BEHAR⁶, AND IOANNIS CONTOPOULOS⁷

May 7, 2015

Received _____; accepted _____

¹Email: fukumukx@jmu.edu

²James Madison University, Harrisonburg, VA 22807

³Astrophysics Science Division, NASA/Goddard Space Flight Center, Greenbelt, MD 20771

⁴Department of Astronomy and CRESST, University of Maryland, College Park, MD 20742

⁵Universities Space Research Association, 7178 Columbia Gateway Dr. Columbia, MD 21046

⁶Department of Physics, Technion, Haifa 32000, Israel

⁷Research Center for Astronomy, Academy of Athens, Athens 11527, Greece

ABSTRACT

We present a study of X-ray ionization of magnetohydrodynamic (MHD) accretion-disk winds in an effort to constrain the physics underlying the highly-ionized ultra-fast outflows (UFOs) inferred by X-ray absorbers often detected in various sub-classes of Seyfert active galactic nuclei (AGNs). Our primary focus is to show that magnetically-driven outflows are indeed physically plausible candidates for the observed outflows accounting for the AGN absorption properties of the present X-ray spectroscopic observations. Employing a stratified MHD wind launched across the entire AGN accretion disk, we calculate its X-ray ionization and the ensuing X-ray absorption line spectra. Assuming an appropriate ionizing AGN spectrum, we apply our MHD winds to model the absorption features in an *XMM-Newton*/EPIC spectrum of the narrow-line Seyfert, PG 1211+143. We find, through identifying the detected features with Fe K α transitions, that the absorber has a characteristic ionization parameter of $\log(\xi_c[\text{erg cm s}^{-1}]) \simeq 5 - 6$ and a column density on the order of $N_H \simeq 10^{23} \text{ cm}^{-2}$, outflowing at a characteristic velocity of $v_c/c \simeq 0.1 - 0.2$ (where c is the speed of light). The best-fit model favors its radial location at $r_c \simeq 200R_o$ (R_o is the black hole innermost stable circular orbit), with an inner wind truncation radius at $R_t \simeq 30R_o$. The overall K-shell feature in the data is suggested to be dominated by Fe XXV with very little contribution from Fe XXVI and weakly-ionized iron, which is in a good agreement with a series of earlier analysis of the UFOs in various AGNs including PG 1211+143.

Subject headings: accretion, accretion disks — galaxies: Seyfert — methods: numerical
— galaxies: individual (PG 1211+143) — X-rays: galaxies

1. Introduction

Blueshifted absorption lines are among the most common spectral features seen in the spectra of accreting compact objects across a large dynamic range in black hole (BH) mass from the supermassive BHs of active galactic nuclei (AGNs) to stellar-mass black holes of galactic binary systems. In the former case, approximately 50% of Seyferts and quasars (QSOs) exhibit absorption signatures in the UV band (e.g. Crenshaw et al. 1999) with a similar fraction ($\sim 50\%$) of Seyfert 1’s showing blueshifted absorption features in their X-ray spectra (Reynolds et al. 1997; George et al. 1998) indicative of an underlying physical link between these two outflow components. A small fraction ($\sim 10\%$) of the radio-quiet QSOs further shows substantially blueshifted UV resonance lines, referred to as broad-absorption-lines (BALs); these are mainly C IV/Mg II (high/low-ionization) at velocities of $v/c \sim 0.04 - 0.1$ where c is speed of light (e.g. Crenshaw et al. 2003).

X-ray spectroscopy plays a fundamental role in the study of AGN absorber properties, because, in distinction to the UV transitions, the X-ray ones span a much wider range in ionization parameter ξ (i.e. the ratio of photon to electron fluxes); thus, within the span of 1.5 decades in photon energy ($\sim 0.3 - 10$ keV) one can sample atomic transitions that cover 5 decades in ξ (e.g. from neutral to Fe XXVI) and presumably a large range in physical length scales. Typically, the so-called X-ray warm absorbers (WAs) have characteristic local columns of $N_H \lesssim 10^{22}$ cm $^{-2}$ and ionization parameter in the range $-1 \lesssim \log \xi \lesssim 4$ at LoS velocities of $v/c \lesssim 0.01$ (e.g. Reynolds & Fabian 1995) presumably originating from sub-pc to pc scales. A rich spectral diversity in soft X-ray regime ($\lesssim 2 - 3$ keV) with a large number of ionic transitions affords the statistical studies of their X-ray absorption line properties (e.g. Behar et al. 2003). Among them, the absorption measure distribution (AMD) can be used as a global measure of the density of the radiation-absorbing gas along a line-of-sight (LoS). AMD is the differential hydrogen-equivalent column N_H per decade of ξ , i.e. $dN_H/d\log \xi$, and it is computed from the measured columns of a variety of ionic species of several elements spanning a large range in ξ (e.g. Steenbrugge et al. 2005; Holczer, Behar & Kaspi 2007; Behar 2009; Detmers et al. 2011). The AMD determination in a number of radio-quiet Seyferts seems to indicate, to zeroth order, a similar global column distribution (i.e. roughly a constant AMD), implying a wind density $n(r)$ that is similar in all of them and decreases like $n(r) \propto r^{-1}$ with radius r (e.g. Detmers et al. 2011; Holczer & Behar 2012).

Furthermore, in recent years, exhaustive X-ray studies of Fe K-shell transitions in AGNs by *XMM-Newton* and *Suzaku* have revealed the presence of another outflowing component in the Seyfert spectra, typically identified as highly-ionized high-Z ions such as Fe XXV/Fe XXVI with H-equivalent columns of $N_H \gtrsim 10^{23}$ cm $^{-2}$, high ionization parameter ($\log \xi \gtrsim 4$) at near-relativistic outflow speeds of $v/c \gtrsim 0.03$, named for this reason ultra-fast outflows (UFOs). The detected UFOs appear to be ubiquitous across both radio-quiet

Seyferts like PG 1211+143 (see also Reeves et al. 2009; Pounds et al. 2003; Pounds & Page 2006; Tombesi et al. 2010a, 2011a, 2012a; Gofford et al. 2013, 2014) and radio-loud ones (e.g. 3C 111 and 3C 120, 3C 390.3, 3C 445) with a likely association of their properties to the radio spectra (Tombesi et al. 2010b, 2011b). The higher X-ray content and increased wind ionization of the latter suggests that strong X-ray photoionization apparently does not inhibit the launch of such fast winds. A detailed study of the properties of X-ray absorbers in a sample of 23 AGN using high resolution X-ray spectroscopy was conducted by Blustin et al. (2005), to conclude that most of the X-ray absorbing matter is launched from large radii (the AGN molecular torus) with kinetic luminosities that are only a small fraction of the AGN budget. In addition to these Seyferts and nearby QSOs, optically/UV-bright broad-absorption-line (BAL) QSOs and their variants (e.g. non-BAL and mini-BAL QSOs) apparently show similar X-ray UFOs but with even higher velocities, up to $v/c \sim 0.7 - 0.8$ in extreme cases¹ such as APM 08279+5255 (Chartas et al. 2002, 2003, 2007, 2009).

PG 1211+143 is a bright quasar at redshift $z = 0.0809$ (Marziani et al. 1996) with X-ray luminosity $\sim 10^{44}$ erg s⁻¹ in 2 – 10 keV band for $H_0 = 75$ km s⁻¹ Mpc⁻¹ and Galactic hydrogen-equivalent column density $N_H = 2.85 \times 10^{20}$ cm⁻² (Murphy et al. 1996). It is an optically bright quasar with a prominent “Big Blue Bump” that results in a relatively steep optical/UV-to-X-ray flux ratio² ($\alpha_{\text{OX}} = -1.45$). Among other spectral features, the first *XMM-Newton*/EPIC/RGS observation of PG 1211+143 in 2001 revealed the first evidence of a highly-ionized UFO with mass flux and kinetic energy comparable to that of the accretion mass rate and bolometric luminosity, respectively (Pounds et al. 2003; Pounds & Reeves 2009), although we note that others have reached different conclusions depending on how to treat the baseline continua (Kaspi & Behar 2006; Gallo & Fabian 2013; Zoghbi et al. 2015). Their analyses detected several strong absorption features identified as blueshifted $K\alpha$ transitions of C, N, O, Ne, Mg, S and Fe. The properties of the Fe feature in particular, imply a wind column density of $N_H \sim 5 \times 10^{23}$ cm⁻² at velocity $v/c \sim 0.08$ and ionization parameter $\log \xi \sim 3.4$. A second observation of PG 1211+143 with *XMM-Newton*/EPIC/RGS in 2004 (Pounds & Reeves 2007) and in 2007 (Pounds & Reeves 2009) have again detected similar UFOs, implying their persistent

¹While the winds of the typical high-velocity UV transition ($L\alpha$, C IV etc.) BALs may be driven by line radiation-pressure, it is a challenge for this scenario to accelerate the highly-ionized, near-relativistic X-ray UFOs.

²The spectral index $\alpha_{\text{OX}} \equiv 0.384 \log(f_{2\text{keV}}/f_{2500})$ measures the X-ray-to-UV relative brightness where $f_{2\text{keV}}$ and f_{2500} are, respectively, 2 keV and 2500 Å flux densities (Tananbaum et al. 1979).

presence despite its highly variable X-ray spectra. A more detailed spectral analysis of such outflows has been recently performed using the *XMM-Newton* data (e.g. Tombesi et al. 2010a, 2011a; Pounds 2014) to confirm their presence, in agreement with the earlier results. Finally, a more recent observation with *Suzaku*/XIS has also revealed the same UFOs as well (Reeves et al. 2008; Patrick et al. 2012; Gofford et al. 2013).

Despite the long-known UV/X-ray WAs combined with an increasing number of statistically-significant detections of the X-ray UFOs, the detailed geometrical structure of these ionized winds, including formation and acceleration processes, are poorly constrained to date. Yet, each of these issues is crucial to the comprehensive picture of accretion-powered phenomena in accretion/outflow physics. Plausible launching mechanisms for general outflows include radiation-driven (e.g. Proga, Stone, & Kallman 2000; Proga & Kallman 2004; Nomura et al. 2013, in the context of UV BALs in luminous QSOs), thermally-driven (e.g. Begelman et al. 1983) and magnetically-driven (e.g. Blandford & Payne 1982; Königl & Kartje 1994, Contopoulos & Lovelace 1994, hereafter CL94; Ferreira 1997; Fukumura et al. 2010a, hereafter FKCB10a; Fukumura et al. 2010b, hereafter FKCB10b; Fukumura et al. 2014, hereafter F14). There have also been hybrid models (e.g. Everett 2005; Ohsuga et al. 2009; Ohsuga & Mineshige 2011; Proga 2003) that attempt to explain an AGN phenomenology associated with inflow and outflow³. With increasingly improved fully-numerical schemes, various extensive simulations have been made in the context of the disk-wind scenario for (i) magnetically driven (e.g. Pudritz et al. 2006; Fendt 2006; Porth & Fendt 2010; Murphy et al. 2010; Stute et al. 2014; Stepanovs & Fendt 2014) and (ii) radiation driven (e.g. Proga & Kallman 2004; Nomura et al. 2013; Higginbottom et al. 2014; Hagino et al. 2015). Although the acceleration mechanism(s) of the observed winds remains uncertain, the magnetic origin seems to be favored over the radiation pressure one according to the latest time-dependent hydrodynamic simulations coupled with multi-dimension Monte Carlo calculations for radiative transfer (e.g., Higginbottom et al. 2014, but also see Hagino et al. 2015) and from UV/X-ray observations (e.g. Kraemer et al. 2005; Everett 2005; Crenshaw & Kraemer 2007). This may also be the case for Galactic binaries (e.g. Miller et al. 2006, 2008; King et al. 2012, 2014). One should note that certain phenomenological outflow models, with emphasis on individual spectral features, such as the Fe K-shell transitions, are able to reproduce the properties of certain prominent transitions such as their EW and their LoS velocity (e.g. Sim 2005; Sim et al. 2008, 2010; Tatum et al. 2012) without providing, however, a global dynamic wind perspective.

To the best of our knowledge, none of the existing wind models, whether semi-analytic or numerical, have so far been able to deliver a practical prescription for the observed X-ray

³The derived values of large ξ , N_H and v of certain X-ray UFOs presumably originating from smaller radii are a serious challenge against line-driven and thermally-driven scenarios.

absorption features; i.e. local properties (i.e. column, ionization state, velocity) of the WAs and UFOs together with a global picture of the outflow physics (i.e. density/ionization structure from smaller scale to larger scales and geometrical properties as a whole). From methodological viewpoint, most models fit the properties of specific features, i.e. column and velocity, implementing `xspec`/`xstar` to obtain the ionization parameter and the velocity of the plasma associated with specific transitions, with little concern on how these fit within a global model of the AGN outflows.

The spirit of our recent works (i.e. CL94; FKCB10a; FKCB10b; Kazanas et al. 2012; F14) has been exactly the opposite, in that we begin with a global MHD wind model and use the X-ray spectroscopic observations to determine the global properties of these winds. In this paper we employ a similar philosophy in an attempt to model the observed Fe XXV UFO in PG 1211+143 within the context of the well-defined MHD-driven wind models referred to above. Our study allows us to constrain explicitly some of the defining MHD wind parameters in the spirit of a *model-driven approach*. Our deeper goal is a better understanding of the underlying physical structure of the observed winds from a global standpoint. Within this framework, WA and UFO features are generically identified as belonging to the same wind structure that spans the entire domain of the AGN accretion disk. We briefly describe the essence of the MHD-driven winds in §2 along with our methodology for constructing a grid of simulated line spectra for subsequent data analysis. In §3 we show our preliminary results based on a 60-ks *XMM-Newton*/EPIC spectrum of PG 1211+143 deriving the best-fit values for the primary model variables. We summarize and discuss the implications of the model in §4.

2. Ultra-fast Outflows in Stratified MHD Disk-Winds

2.1. The Magnetized Disk-Wind Structure

Following FKCB10a and FKCB10b for the computational prescription of magnetically-driven disk-wind models under steady-state, axisymmetric conditions, we seek new insight into their structure from the observational data. We apply our model assuming the observed X-ray UFO signatures in AGNs (i.e. Fe XXV/Fe XXVI resonance transitions)⁴ are produced by X-ray photoionization of MHD winds launched off of an accretion disk. The detailed characteristics of the model discussed in FKCB10a and FKCB10b will be briefly described

⁴The model, however, is not restricted to Fe K-shell transitions and can be extended in general to include other ionic features detected in AGNs and black hole binaries.

here. Geometric and physical properties of the wind in the model are primarily governed by two conserved quantities along a wind streamline, namely the particle-to-magnetic flux ratio F_o and angular momentum H_o . The former one, F_o , determines predominantly the wind kinematics and the latter, H_o , generally dictates the global wind structure in the poloidal plane. The fundamental quantity of axisymmetric MHD is the magnetic stream function $\Psi(r, \theta)$, assumed to have a self-similar form $\Psi(r, \theta) \equiv (R/R_o)^q \tilde{\Psi}(\theta) \Psi_o$, with Ψ_o the poloidal magnetic flux through the fiducial innermost disk radius at $R = R_o$. $\tilde{\Psi}(\theta)$ is its angular dependence to be solved for and q is a free parameter that determines the radial dependence of the poloidal current. The scalings of the poloidal magnetic stream function carry over to the rest of the wind properties of which we show only the magnetic field, velocity and density

$$\mathbf{B}(r, \theta) \equiv (R/R_o)^{q-2} \tilde{\mathbf{B}}(\theta) B_o, \quad (1)$$

$$\mathbf{v}(r, \theta) \equiv (R/R_o)^{-1/2} \tilde{\mathbf{v}}(\theta) v_o, \quad (2)$$

$$n(r, \theta) \equiv (R/R_o)^{2q-3} \tilde{n}(\theta) B_o^2 v_o^{-2} m_p^{-1}, \quad (3)$$

with the momentum-balance equation

$$\rho(\mathbf{v} \cdot \nabla) \mathbf{v} = -\nabla p - \rho \nabla \Phi_g + \frac{1}{c} (\mathbf{J} \times \mathbf{B}), \quad (4)$$

where m_p is the proton mass and ρ is plasma mass density.

The dimensionless angular functions denoted by *tilde* must be obtained from the conservation equations and the solution of the Grad-Shafranov equation (the force balance equation in the θ -direction) with initial values on the disk (denoted by the subscript “o”) at $(R = R_o, \theta = 90^\circ)$. The density normalization at $(R_o, 90^\circ)$, setting $\tilde{n}(90^\circ) = 1$, is given in terms of the dimensionless mass-accretion rate \dot{m}_a (normalized to the Eddington accretion rate $\dot{M}_E = L_E/c^2$, see FKCB10a) by

$$n_o \equiv \frac{\tau(\dot{m}_a) f_w}{\sigma_T R_S}, \quad (5)$$

where σ_T is the Thomson cross-section, f_w is the ratio of the outflow rate in the wind to \dot{m}_a and R_o is assumed to be on the order of the Schwarzschild radius R_S . The Thomson depth $\tau(\dot{m}_a)$ of the plasma at the innermost disk radius is further scaled by the dimensionless mass-accretion rate \dot{m}_a with normalization τ_o as $\tau(\dot{m}_a) \equiv \dot{m}_a \tau_o$, which leads to

$$n_o \equiv \frac{f_w \dot{m}_{a,o}}{\sigma_T R_S} = 5 \left(\frac{f_w \dot{m}_{a,o}}{M_8} \right) \times 10^{11} \text{ cm}^{-3}. \quad (6)$$

where we have introduced an effective mass-accretion rate $\dot{m}_{a,o} \equiv \dot{m}_a \tau_o$ as it is difficult to decouple one from the other from observations. In this paper we consider one of the fiducial wind solutions, model (A), from Fukumura et al. (2014), as a baseline wind model, by

choosing $q = 0.93$ (i.e. $n \propto r^{-1.14}$), $f_w = 1$ and $\tau_o = 10$ representing an optically-thick disk of $\dot{m}_{a,o} = 10$ at $R = R_S$ (low case r denotes the radial distance in 3-space, while R along the disk surface). Here, we only highlight the essence of the model; details can be found elsewhere (CL94; FKCB10a,b; Kazanas et al. 2012; F14). Formally the self-similar winds extend from $r = 0$ to $r \rightarrow \infty$, however, physical considerations restrict these to a finite but broad range in r . So we choose the dimensionless factors f_t, f_T to denote the inner and outer truncation radii of our winds on the disk surface by

$$R_t \equiv f_t R_S, \quad R_T \equiv f_T R_S \quad (7)$$

where the value of f_t is to be constrained by the X-ray data while $f_T \gg 1$, **typically** $\sim 10^6$. Once launched, the asymptotic wind speed in this solution is found to be $v_p/v_o \sim 4$ at $r/R_S \lesssim 10^3$ (see F14 for details).

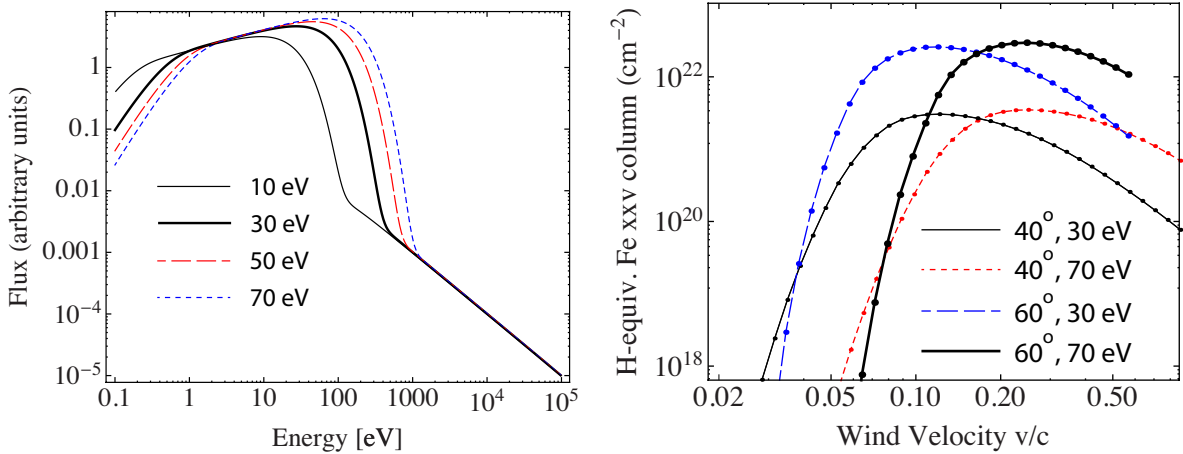


Fig. 1.— (a) Input ionizing SED for photoionization calculations for the MCD of $kT_{\text{bbb}} = 10, 30, 50$ and 70 eV with $\alpha_{\text{OX}} = -1.5$ and $\Gamma = 2$. (b) An example of calculated Fe XXV (hydrogen-equivalent) local column distribution \mathcal{N}_H for different sets of $(\theta, kT_{\text{bbb}})$ as labeled.

2.2. Photoionization of Disk-Winds

With the dimensionless, mass-invariant wind structure for a given $\dot{m}_{a,o}$ and a viewing angle θ , the only significant difference in the wind ionization properties across objects of different luminosity comes from the spectral energy distribution (SED) of the accretion-powered luminosity $L \equiv \dot{m}_a L_E \epsilon$ where $L_E = 1.25 \times 10^{46} M_8 \text{ erg s}^{-1}$ is the Eddington luminosity with M_8 the black hole mass in units of $10^8 M_\odot$ and $\epsilon \simeq 0.1$ is the

accretion efficiency. While in FKCB10a we used a simple power-law spectrum of the form $F_\nu \propto \nu^{-1}$ (e.g. Sim et al. 2008, 2010), here we consider a multi-component SED consisting of a multicolor-disk (MCD) with an innermost temperature of kT_{bbb} and an X-ray power-law of photon index Γ (with a low-energy cut-off at 50 eV and a high-energy turnover at 200 keV) normalized to the MCD by α_{OX} (e.g. Everett 2005; Sim 2005), a more appropriate SED for bright Seyferts such as PG 1211+143. The ionizing luminosity (X-ray plus EUV) is then $L_{\text{ion}} \simeq 0.1L \simeq 1.25M_8 \times 10^{44} \text{ erg s}^{-1}$ for a relatively high accretion rate of $\dot{m}_a = 1$ as suggested in the earlier analyses (e.g. Pounds et al. 2003).

For a characteristic Seyfert SED, we set $\Gamma = 2$ (see Fig. 5 in Tombesi et al. 2011a for a homogeneous sample of 42 radio-quiet AGNs and Pounds & Reeves 2009) and $\alpha_{\text{OX}} = -1.5$ (adopted from NED and Blustin et al. 2005) while leaving an inclination angle θ and the disk temperature kT_{bbb} as free parameters to be determined by PG 1211+143 UFO observations (e.g. Pounds et al. 2003; Tombesi et al. 2011a). It should be noted that, in agreement with FKCB10b, Blustin et al. (2005) find that only more negative values of α_{OX} allow higher velocity absorbers (i.e. $v_{\text{out}} \gtrsim 10,000 \text{ km s}^{-1}$) based on their analysis of phenomenological and physical properties of the detected warm absorbers using high-resolution X-ray spectroscopy of a sample of Seyfert 1 type AGNs.

Given the wind density normalization n_o through $\dot{m}_{a,o}$, photoionization balance is computed radially outward employing **xstar** (Kallman & Bautista 2001, v2.2.1bn13) by setting the SED of Fig. 1a as the ionizing spectrum at the innermost radius; the radiation transport in the wind is done by discretizing the radial wind coordinate using a large number of cells in radial direction for a given angle θ (typically with $\Delta r/r \sim 0.1$ allowing to treat each radial cell as a plane, yielding 50-70 radial zones; see FKCB10a). We apply **xstar** in the first zone to compute the ionization equilibrium of the plasma and also its opacity and emissivity. Then we use the output of this zone as input for the next one and continue to the outer edge of the wind along a given LoS (i.e. a given θ). We calculate the absorption spectra with the Voigt function (e.g. Mihalas 1978; Kotani et al. 2000; Hanke et al. 2009) defined as

$$H(a, u) \equiv \frac{a}{\pi} \int_{-\infty}^{\infty} \frac{e^{-y^2} dy}{(u - y)^2 + a^2} . \quad (8)$$

where we use $a \equiv \Gamma_E/(4\pi\Delta\nu_D)$ with Γ_E being the Einstein coefficient and $\Delta\nu_D$ the line Doppler broadening factor. The dimensionless frequency spread about the transition frequency ν_o is given by $u \equiv (\nu - \nu_o)/\Delta\nu_D$. Note that, in order to compute the flux in lines whose thermal width is narrower than the computational frequency grid (especially in cases of multiple lines within a given frequency spacing), the parameter **vturb** (typically $\sim 1000 \text{ km/s}$) of **xstar** is employed to provide line width $\Delta\nu_D$ consistent with the produced flux over the grid size. However, our wind model provides, instead, a well-defined velocity shear ΔV with a corresponding radial velocity difference Δv_D between two adjacent radial

cells; we employ this velocity instead of `vturb` to define an equivalent $\Delta\nu_D = \nu_0(v_D/c)\Delta v_D$, a value consistent with the underlying wind kinematics (see FKCB10a for a detailed numerical prescription).

Using the ionic column $N_{\text{ion}}(r; \theta)$ over a radial cell of width Δr as a function of ionization parameter $\xi(r; \theta)$ obtained with `xstar` under ionization and heating-cooling balance, we can compute the wind opacity $\tau_\nu(r, \theta)$ of any given photon energy and at any given point with wind velocity $v(r; \theta)$ from the relation

$$\tau_\nu(r, \theta) = \sigma_{\text{photo}, \nu}(r, \theta) N_{\text{ion}}(r, \theta) , \quad (9)$$

where the line photoabsorption cross section $\sigma_{\text{photo}, \nu}$ at frequency ν is given by

$$\sigma_{\text{photo}, \nu} \equiv 0.001495 \frac{f_{ij} H(a, u)}{\Delta\nu_D} \text{ cm}^2 , \quad (10)$$

and f_{ij} is the oscillator strength of the transition between the i -th and j -th levels of an ionic species. Finally, we construct a two-dimensional grid of baseline spectra for $\theta \in [30^\circ, 70^\circ]$ and $kT_{\text{bbb}} \in [10\text{eV}, 70\text{eV}]$ for density normalization⁵ $n_o = 5.1 \times 10^{11} \text{ cm}^{-3}$ ($\dot{m}_{a,o} = 10$). Here we introduce the quantity \mathcal{N}_H defined as the number density of Fe XXV ions divided by the Fe abundance and multiplied by the width of our local radial grid size Δr . Some of the calculated \mathcal{N}_H (assuming solar abundances) for four sets of θ and kT_{bbb} are shown as a function of the wind velocity v/c in Figure 1b. Considering this figure, it is reminded that the velocity decreases with increasing distance r and decreasing ionization parameter ξ for a given LoS angle θ . The reader should note that \mathcal{N}_H does not depend monotonically on velocity because, at small r (and high v), a good fraction of Fe is fully ionized, while at larger distances (i.e. low velocities) the Fe ionization drops precipitously. Finally, the *total* \mathcal{N}_H , $N_H(\text{Fe XXV})$, is found by integrating \mathcal{N}_H over r along a given LoS. As seen, for a given $\dot{m}_{a,o}$, the normalization of the LoS column depends primarily on the inclination θ while the location of peak \mathcal{N}_H (i.e. where \mathcal{N}_H is maximum), for a given α_{OX} and n_o , is mainly determined by the disk temperature kT_{bbb} . Such a correlation is also discussed in FKCB10b.

2.3. A Spectral Grid of mhdwind Models

For the model described in §2.1-2.2 and with the density normalization fixed at $n_o = 5 \times 10^{11} \text{ cm}^{-3}$ at $\theta = 90^\circ$ (i.e. $\dot{m}_{a,o} = 10$) we construct a grid of `mhdwind` models

⁵Note that the wind density $n(r, \theta) \propto f(r)g(\theta)n_o$ has both *radial* $f(r)$ and *angular* $g(\theta)$ dependencies. $g(\theta)$ (Fig. 2a of FKCB10a) decreases by factor of $\sim 10^4$ for $0^\circ \leq \theta \leq 90^\circ$.

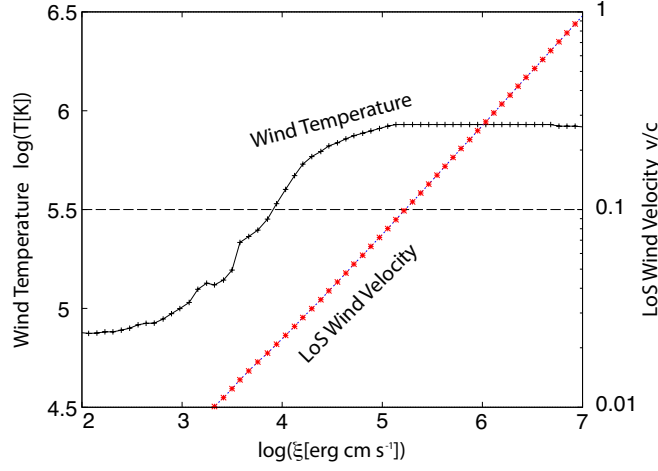


Fig. 2.— Radial profiles for photoionized wind temperature $\log(T[\text{K}])$ (on the left ordinate) and velocity v/c (on the right ordinate) as a function of ionization parameter ξ for $\theta = 50^\circ$ and $kT_{\text{bbb}} = 30$ eV.

by varying the three parameters $(\theta, kT_{\text{bbb}}, f_t)$. By solving the radiative transfer along radial rays with the wind photoionization as described above we first obtain the column distribution for FeXXV and FeXXVI in the ionized wind as a function of ionization parameter $\xi(r, \theta)$ or equivalently **as** a function of **the** wind velocity v along a given LoS angle θ (see FKCB10a,b) as shown in Figure 1b. A different aspect of the wind is shown in Figure 2 where we demonstrate the wind velocity $v(\xi)$ and temperature $T(\xi)$ under ionization balance for $\theta = 50^\circ$ and $kT_{\text{bbb}} = 30$ eV. The wind velocity in this framework scales like $v \propto r^{-1/2}$ as discussed in FKCB10a, FKCB10b and F14. A sample grid of the simulated FeXXV absorption line profiles is shown in Figure 3a for various combinations of $(\theta, kT_{\text{bbb}}, R_t)$ within the range considered here. As seen, the dependence on each parameter can be probed by the spectral shape in terms of the depth of trough and line shift. A comparison between FeXXV and FeXXVI is shown in Figure 3b where we explore the spectral variations for different truncation radius $f_t \equiv R_t/R_o$ by setting $kT_{\text{bbb}} = 40$ eV and $\theta = 50^\circ$. One should note that the small fluctuations in the model line profiles in Figure 3 is not real and caused by the size of the radial bin we choose in our model.

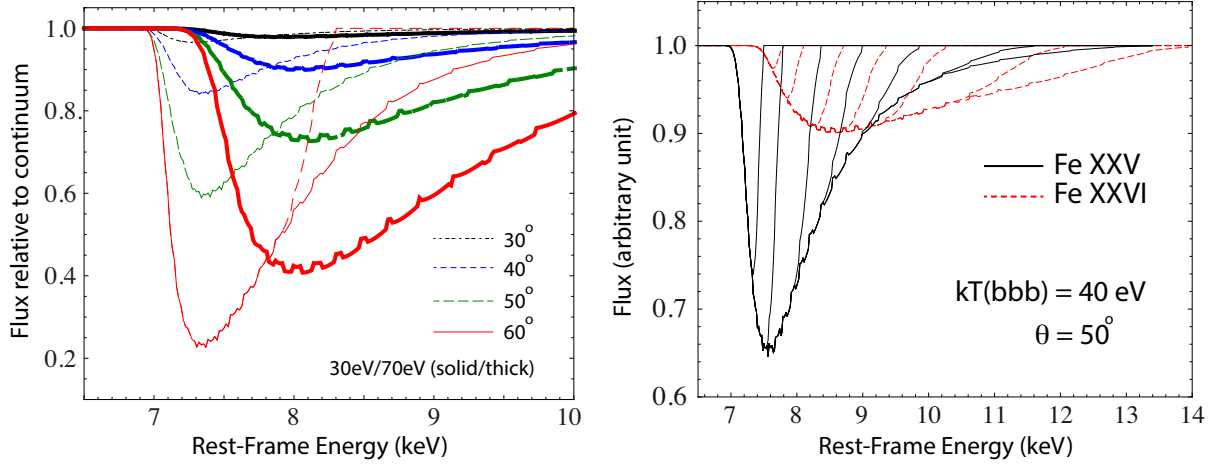


Fig. 3.— (a) Simulated Fe xxv absorption features illustrating the diagnostic capability of our model for $\theta = 30^\circ, 40^\circ, 50^\circ$ and 60° (from top to bottom) with thin curves denoting an input thermal disk spectrum with $kT_{bbb} = 30$ eV and thick curves being 70 eV. The dashed curve is given by $kT_{bbb} = 30$ eV but for $R_T/R_o = 10$. (b) A similar K-shell feature due to Fe xxv (black) and Fe xxvi (red) for various truncation radii R_T as listed in Table 1.

3. Preliminary Comparison with the PG 1211+143 Data

3.1. *XMM-Newton*/EPIC Data

We use an *XMM-Newton* spectrum of PG 1211+143 (obsID: 0112610101) obtained with the EPIC-pn camera for an approximately 60-ks duration on 2001 June 15 (Pounds et al. 2003), for which a detailed data reduction procedure and observed spectral and temporal features of this object can be found elsewhere (e.g, Pounds et al. 2003; Pounds & Page 2006; Kaspi & Behar 2006; Tombesi et al. 2011a; Bachev et al. 2009; Pounds & Reeves 2009; Gallo & Fabian 2013; Pounds 2014, reference therein). Earlier analyses of the UFOs, typically identified as either Fe xxv and/or Fe xxvi, seem to imply an estimate on the column density of $N_H \sim 10^{23} \text{ cm}^{-2}$, velocity of $v/c \sim 0.1 - 0.15$ and ionization parameter of $\log \xi \sim 3 - 5$, although an alternative view may also be conceivable claiming that the observed Fe K absorption feature can be attributed to several consecutive low charge states of Fe (see, e.g., Kaspi & Behar 2006).

Table 1. Model Grid of `mhdwind` Component

Primary Parameter	Range
Viewing Angle θ (degrees)	$30^\circ, 40^\circ, 50^\circ, 60^\circ, 70^\circ$
BBB Disk Temperature kT_{bbb} (eV)	10, 30, 50, 70
Disk Truncation Radius $\log f_t \equiv \log(R_t/R_o)$	0, 0.3, 0.6, 0.9, 1.2, 1.5, 1.8

Assume $M_8 = 1$, $\alpha_{\text{ox}} = -1.5$, $\Gamma = 2$, $n_o = 5 \times 10^{11} \text{ cm}^{-3}$ and $L_{\text{ion}} = 1.25 \times 10^{44} \text{ erg s}^{-1}$.

3.2. Spectral Modeling for the Fe K α UFO

Here we perform a spectral analysis of the UFOs previously detected in the 60 ks *XXM-Newton*/EPIC spectrum of PG 1211+143 (e.g. Pounds et al. 2003; Pounds & Reeves 2009; Tombesi et al. 2011a). Focusing on the hard X-ray absorption feature identified as Fe K-shell resonance transition in the data, we implement our MHD-wind model, **mhdwind**, into **xspec** as a multiplicative table model as discussed in §2. We follow the analysis procedure in Tombesi et al. (2011a) where the 2 – 10 keV band is modeled with an underlying continuum power-law (**po**). To fit the Fe K α absorber, however, we replace the phenomenological **xstar** component by our MHD-wind model **mhdwind**. The symbolic spectral form reads as “**phabs*(po+zga)*mtable{mhdwind}**” where we have used the previously estimated values of parameters, Galactic absorption due to neutral hydrogen column (**phabs**) $N_H = 2.85 \times 10^{20} \text{ cm}^{-2}$ (Murphy et al. 1996), $\Gamma = 2$ (Tombesi et al. 2011a), and black hole mass, $M = 10^8 M_\odot$, based on the earlier estimates (Kaspi et al. 2000; Bentz et al. 2009). Attributing the pronounced emission line at ~ 6.5 keV (in the rest-frame) to fluorescence from the disk, our **mhdwind** is constrained simultaneously with a red-shifted gaussian component **zga** of XSPEC in which the line width is set to be $\sigma_{\text{Fe}} = 0.15$ keV whose exact value has little influence on our end results.

We explore two cases by simultaneously considering both the Fe XXV and Fe XXVI transitions: Model (A), where, R_t , the innermost radial extent of the wind at $\theta = 90^\circ$, is equal to $R_o \simeq R_S$ and model (B) where this restriction is relaxed. Figure 4a shows the best-fit for each of models (A) and (B) in comparison with the no **mhdwind** model. We set $n_o = 5 \times 10^{11} \text{ cm}^{-3}$ ($m_{a,o} = 10$) while varying θ , kT_{bbb} and f_t . The best-fit values are listed in Table 2. We have used different values of n_o in our calculations but its effective role is to change slightly the depth of the trough. In the current wind model, both visual and statistical inspection favors model (B) by $\Delta\chi^2 = 2.3$ (table 2) in which the wind does not originate at the fiducial radius R_o on the disk surface, but at $R_t = f_t R_S$ with $f_t > 1$.

In model (A), where $f_t = 1$ is assumed, we obtain our best-fit for values $\theta = 40^\circ$ (pegged) and $kT_{\text{bbb}} = 30$ eV with $\chi^2/\nu = 200.84/129$ with **mhdwind** which is a statistically significant addition to the continuum (with an improvement of $\Delta\chi^2 = 34.1$ for two additional parameters). In model (B) we relaxed the restriction on the wind truncation radius $f_t = 1$ of model (A). Table 3 shows a list of various characteristic radii in this model. Our analysis yields a best-fit model with $\theta = 50^\circ$, $kT_{\text{bbb}} = 38$ eV and $f_t = 10^{1.48}$, as shown in Figure 4a and Table 2, where we obtain $\chi^2/\nu = 198.54/128$ which is more significant in comparison with model (A). We note that the model spectrum now has a sharper edge on the bluer side of the feature as required in data. The total column, $\mathcal{N}_H = 1.2 \times 10^{23} \text{ cm}^{-2}$ from model (B) is comparable to the previous estimate with **xstar** model although our wind is continuous rather than discrete.

As a measure of assessing the Fe XXV absorption wind properties we first calculate a

Table 2. Summary of our best-fit `mhdwind` model parameters for PG 1211+143.

Parameter/Model	Model (A) Fe xxv/Fe xxvi	Model (B) Fe xxv/Fe xxvi
θ [degree]	40.0 \diamond	$49.8^{+3.27}_{-6.52}$
kT_{bbb} [eV]	$30.1^{+9.01}_{-2.56}$	$38.1^{+4.55}_{-9.01}$
E_{Fe} [keV]	$6.54^{+0.097}_{-0.080}$	$6.52^{+0.10}_{-0.073}$
τ_{max}	$0.095^{+0.014}_{-0.0105}/0.019^{+0.0023}_{-0.0031}$	$0.235^{+0.073}_{-0.124}/0.052^{+0.018}_{-0.024}$
$\log(r_c/R_S)^{\flat}$	$2.96^{+0.116}_{-0.161}/2.51^{+0.11}_{-0.16}$	$2.37^{+0.48}_{-0.35}/1.82^{+0.54}_{-0.25}$
$\log(\xi_c[\text{erg cm s}^{-1}])^{\triangle}$	$5.21^{+0.149}_{-0.104}/5.62^{+0.147}_{-0.105}$	$5.31^{+0.13}_{-0.15}/5.80^{+0.084}_{-0.17}$
v_c/c^{\triangle}	$0.099^{+0.023}_{-0.008}/0.165^{+0.038}_{-0.013}$	$0.115^{+0.016}_{-0.021}/0.208^{+0.018}_{-0.043}$
$\mathcal{N}_{\mathcal{H}}$ [cm $^{-2}$] /10 22 \sharp	$4.04^{+0.224}_{-0.178}/5.94^{+0}_{-0.182}$	$12.1^{+5.30}_{-7.56}/16.7^{+5.72}_{-8.63}$
$\log(R_t/R_S)$	0 \clubsuit	$1.48^{+0.065}_{-0.27}$
χ^2/ν (with <code>mhdwind</code>)	200.84/129	198.54/128
$\Delta\chi^2$ (from <code>phabs*(po+zga)</code>)	-34.1	-36.4

\diamond The value is pegged.

\flat The characteristic LoS radius r_c where wind Fe xxv opacity τ_{ν} (see eqn. (9)) is maximum along a given LoS angle.

\triangle The characteristic value (“c”) is evaluated at the LoS position $r = r_c$.

\sharp LoS-integrated total Fe xxv column density.

\clubsuit The value is fixed.

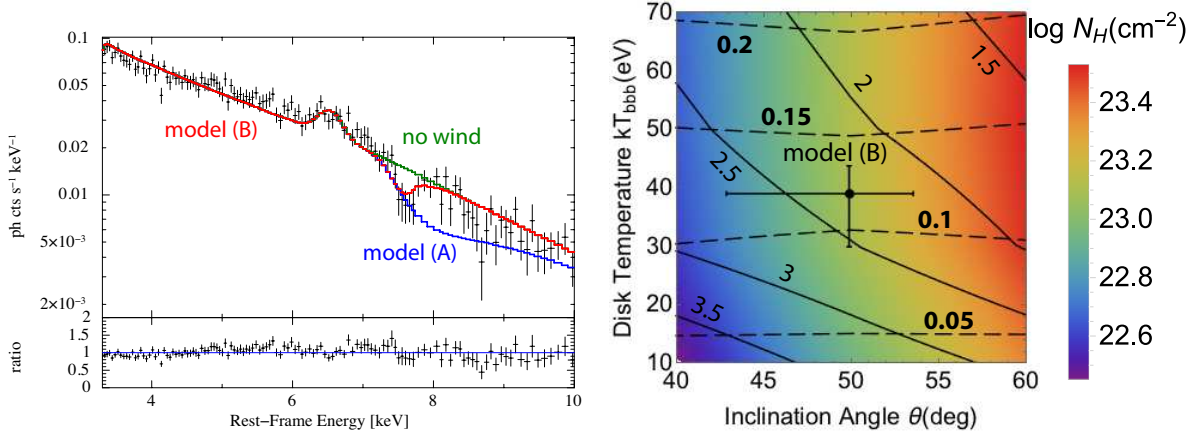


Fig. 4.— (a) 60 ks *XMM-Newton*/EPIC-pn spectrum of PG 1211+143 fitted with model (A) (blue) and (B) (red) in comparison with no `mhdwind` component (in green) varying three primary parameters $(\theta, kT_{\text{bbb}}, f_t)$ with $n_o = 5 \times 10^{11} \text{ cm}^{-3}$ (i.e. $\dot{m}_{\text{a,o}} = 1$). (b) Calculated contours for characteristic radius $\log(r_c/R_S) = 1.5, 2, 2.5, 3, 3.5$ (solid; upper right to lower left) and wind velocity $v_c/c = 0.2, 0.15, 0.1, 0.05$ (dashed; top to bottom) with the best-fit Fe XXV column in model (B). Color indicates the net Fe column density \mathcal{N}_H . See Table 2 for details.

characteristic radius R_c at which the wind photoelectric absorption column for the Fe XXV transition becomes maximum for a given LoS inclination angle θ . At this radius we compute the other physical quantities listed in Table 2. Notice that the *total* \mathcal{N}_H (in units of 10^{22} cm^{-2}) is defined as the local column density integrated over the LoS distance.

Along the LoS of the values of θ obtained by our fits (see Table 2), the wind is both Thomson thin and also thin at the Fe energies. Because, as argued earlier, the Fe XXV/Fe XXVI line opacities are non-monotonic functions of the radial coordinate in these directions, we define a radius r_c along each of these LoS at which the line(s) opacity (ies) is (are) maximized (given by the entry τ_{max} of Table 2). In fact, these coincide with the maxima of \mathcal{N}_H of Fig. 1b. Because of the smoothness and continuity of \mathcal{N}_H with r , ξ or v , the absorption of X-ray photons begins at $r \ll r_c$ and extends over more than one decade in radius. One should hence bear in mind that a given absorption feature in our models does not correspond to specific, unique wind component.

In order to examine in more detail the multi-parameter space spanned by $(\theta, kT_{\text{bbb}})$ we interpolate the wind variables such as velocity v_c and characteristic radius r_c as shown

in Figure 4b where color shows total column $\log(\mathcal{N}_{\mathcal{H}}[\text{cm}^{-2}])$ for Fe XXV with contours of radius $\log(r_c/R_o)$ (solid), and contours of v_c/c (dashed). The best-fit model (B) for Fe XXV is indicated by a dark dot. It should be reminded that the best-fit characteristic values (i.e. r_c, v_c, ξ_c) are simply constrained at the most opaque radius ($\tau_{\text{max}} \equiv \tau(r = r_c)$) of the absorber. The neighboring plasma at $r \lesssim r_c$ (i.e. $v \gtrsim v_c$) and $r \gtrsim r_c$ (i.e. $v \lesssim v_c$) contributes also progressively to the formation of the absorption feature thus there is no *single* wind velocity nor column density in our model. *This is a characteristic feature of the continuous wind model which is fundamentally different from a single-component absorber model often employed in a phenomenological analysis.* The corresponding confidence contours for model (B) are shown in Figure 5 where the primary variables θ, kT_{bbb} and f_t are constrained.

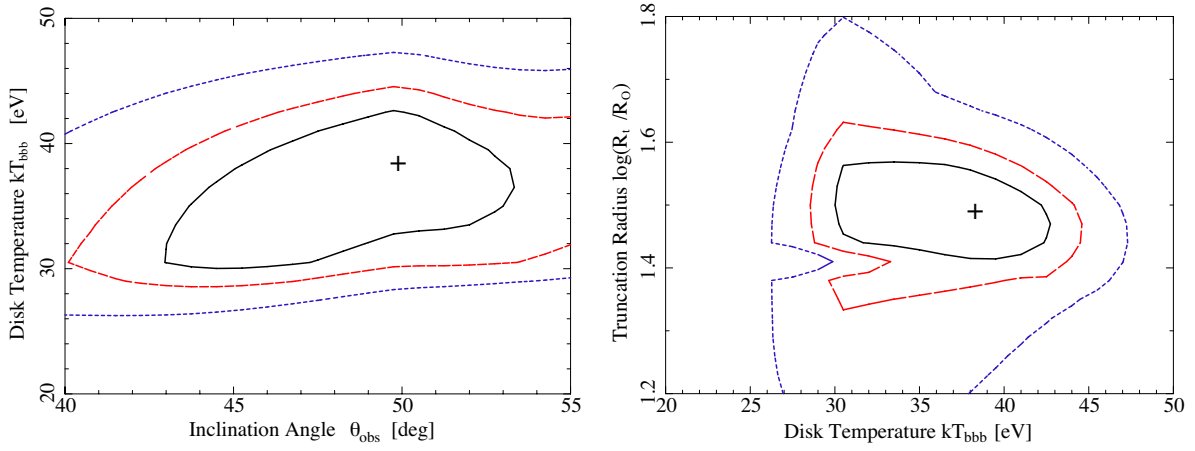


Fig. 5.— Confidence contour plots for (a) temperature kT_{bbb} and inclination θ and (b) truncation radius R_t and temperature kT_{bbb} at the confidence level of 68%, 90%, and 99% also indicated by the best-fit model (B) (cross). See Table 2 for details.

In the context of the current model, the best-fit model (B) is spatially identified as illustrated in Figure 6a where the calculated fiducial wind structure in the vicinity of the black hole is superimposed showing the normalized number density $n(r, \theta)$ in color, the velocity field (white arrows), the magnetic field lines (solid thick), the contours for density (dashed) and the Alfvén surface (white line). In this simplified approach a geometrically-thin disk is situated in the equatorial plane at $\theta = \pi/2$. As discussed earlier, the faster portion of the modeled Fe XXV/Fe XXVI absorber (i.e. the bluer side of the trough) and the slower one (i.e. the redder one) are respectively located at $r < r_c$ and $r > r_c$ along each LoS and they all progressively contribute to produce the observed absorption feature (both in depth and width).

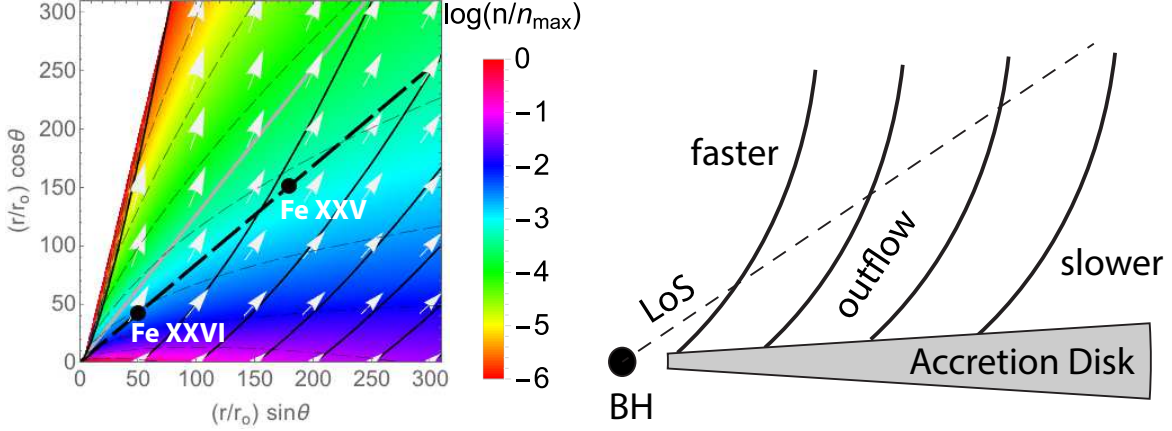


Fig. 6.— (a) Geometrical identification of the observed Fe XXV/Fe XXVI from *XMM-Newton*/EPIC spectrum of PG 1211+143 with *mhdwind* model (B). We show the global magnetic field lines (thick solid), normalized wind density $\log(n(r, \theta)/n_{\max})$ in color and its contours (dashed), velocity field (white arrows) along with the inferred location of Fe XXV and Fe XXVI. See Table 2 for details. (b) A schematic to illustrate the MHD-driven AGN winds.

In terms of the energy budget of the observed UFO, by using the outflow density profile with $n \propto 1/r$ (in the present model actually $n \propto 1/r^{1.14}$) in this work for a supermassive black hole mass of $M = M_8$ (Kaspi et al. 2000; Peterson et al. 2004), a mass-outflow rate associated with the Fe XXV line can be estimated as

$$\dot{M}_{\text{out}}(\text{Fe XXV}) \equiv 2\pi b m_p \int_0^{200} n(r, \theta) v_z(r, \theta) r dr, \quad (11)$$

$$\sim 4\pi b m_p n_o c R_S^2 v_{\text{Fe XXV}} x_{\text{Fe XXV}}^{1/2}, \quad (12)$$

$$\sim 2.56 M_\odot \text{ yr}^{-1} \left(\frac{b}{0.4} \right) \left(\frac{n_o}{5 \times 10^{11}} \right) \left(\frac{M}{10^8 M_\odot} \right) \left(\frac{v_{\text{Fe XXV}}}{0.1} \right) \left(\frac{x_{\text{Fe XXV}}}{200} \right)^{1/2} \quad (13)$$

where $x \equiv r/R_S$ and the upper limit of integration is indicative of the distance to Fe XXV location; i.e. $r_c = r_{\text{Fe XXV}}$ (see tab. 2). This value is consistent with the earlier estimate of $\sim 3 M_\odot \text{ yr}^{-1}$ (Pounds et al. 2003; Pounds & Page 2006). Since the corresponding local mechanical power is given by

$$\dot{E}_{\text{out}}^{(\text{local})} \equiv \dot{M}^{(\text{local})} v_{\text{out}}^2 \propto r^{-1/2}, \quad (14)$$

the local kinetic power of the Fe XXV outflow is dominated by the inner outflow radius R_t

yielding

$$\dot{E}_{\text{out}}(\text{Fe XXV}) \sim \frac{1}{2} \dot{M}_{\text{out}}(\text{Fe XXV}) v_{\text{Fe XXV}}^2 \sim 2 \times 10^{44} \text{ erg s}^{-1}, \quad (15)$$

a value comparable to power the observed X-ray luminosity $\sim 10^{44} \text{ erg s}^{-1}$ (Pounds et al. 2003) also potentially providing a large impact on AGN feedback process at large scales (e.g. Crenshaw & Kraemer 2012). A similarly large outflow power has been made, for example, to other bright AGNs such as PDS 456 (Reeves et al. 2003; Nardini et al. 2015).

4. Summary & Discussion

We have demonstrated, by modeling its *XMM-Newton* spectrum, that MHD-driven winds with $n \propto r^{-\alpha}$, $\alpha \simeq 1$, originally proposed to account for the X-ray WAs in Seyferts, can also encompass the UFOs, *i.e. the high-velocity X-ray absorbers* of the bright Seyfert PG 1211+143. The absorber’s properties of PG 1211+143 as manifest by the Fe XXV/Fe XXVI transition properties, are determined mainly by the wind mass flux $\dot{m}_{\text{a,o}}$, the disk temperature kT_{bbb} and the observer’s viewing angle θ . By producing a grid of model K-shell Fe absorption lines, appropriate to photoionized MHD winds, we found that the absorbers’ physical conditions are well constrained by our models. Thus the Fe XXV and Fe XXVI properties are respectively given by the location of maximum opacity at $r_c/R_S = 234$ and 66, LoS velocity $v_c/c = 0.115$ and 0.208, ionization parameter $\log \xi_c = 5.31$ and 5.80, total H-equivalent columns $\mathcal{N}_H = 1.21 \times 10^{23} \text{ cm}^{-2}$ and $1.67 \times 10^{23} \text{ cm}^{-2}$, with the wind truncated at radius $f_t \equiv R_t/R_S = 10^{1.48} \approx 30$. While the best-fit values of these parameters are roughly consistent with the earlier analysis (e.g. Gofford et al. 2013), our model can further provide a geometrical and physical identification of the UFO in PG 1211+143 data rather than phenomenological interpretation as illustrated in Figure 6b. In fact, a recent discovery of the unambiguous P-Cygni-like profile of the UFOs made by simultaneous X-ray observations with *XMM-Newton* and *NuSTAR* of a similar luminous quasar, PDS 456, indicates a similar spherically-extended wind geometry rather than a narrow collimated radial streamline (Nardini et al. 2015) in consistence with our MHD-driven view discussed for PG 1211+143.

Although in this paper we are focusing on the origin of the detected Fe $K\alpha$ UFOs, our model winds extend over a large range in r, ξ and v . As such, they imply the presence of other charge states that contribute to the Fe $K\alpha$ transition by including Fe XVIII–Fe XXIV. We found that should these additional states be included in our analysis, the Fe $K\alpha$ feature would have been much broader than seen in the data. Given our fits of Fig. 4a and Table 2, one must surmise that the effective contribution to 1s–2p transition from Fe XVIII through Fe XXIV in the data ought to be very small (if not none). There are a number of remedies:

(i) It is conceivable that the intrinsically broad absorption feature due to ionized iron at all charge states could be externally filled by scattered resonant line photons which would suppress its otherwise broader signature. Any continuous wind model will inevitably come across this issue of the contribution of states other than highly-ionized (e.g. H/He-like) ones. (ii) The radial wind density profile might be steep enough to suppress the ionic column at large distances. On the other hand, this solution may not be consistent with the observed slow absorbers (i.e. warm absorbers) since they originate from large distances in this model. (iii) It is also probably that the fast absorbers (i.e. UFOs) could be a collection of discrete (small) gas clouds along the LoS instead of a large-scale continuous flow (e.g. Misawa et al. 2014) that might also be in a constant pressure equilibrium causing the suggested thermal instability (e.g. Holczer, Behar & Kaspi 2007). While we note this long-standing question, this is beyond the scope of our current study.

To compute the spectra of a truncated wind, we simply removed the contribution to the line feature by the self-similar section of the wind that originates at $R < f_t R_S$. We also repeated the photoionization of a wind in which this section has already been removed, assuming always that the ionizing source is located at $r = 0$. This second calculation produced similar results with slightly smaller values for \mathcal{N}_H , because of the slightly larger flux of ionizing radiation at the values of θ considered. This could be ameliorated by a slight increase in the value of n_o . The constrained truncation radius $R_t \approx 30 R_S$ in Table 2 is statistically favored in the context of our MHD-wind model particularly so as to suppress the blue tail of the absorption feature. On the other hand, Giustini & Proga (2012), for example, have considered a thermally-driven wind based on the model of Luketic et al. (2010). They found a relatively sharp blue edge of the line profile without truncation due to non-monotonic profiles for wind streamlines and opacity along a LoS. This implies that a complex geometry of the wind also needs to be further explored by extending the model beyond self-similar limit.

It is suggested from a long *Suzaku* observation that a similar fast X-ray absorber (by iron K-shell transition at an implied outflow velocity of $v \sim 0.25c$) in PDS 456 exhibits rapid variability as short as ~ 1 week (Gofford et al. 2014). Their estimate of the absorber’s location in PDS 456 ($r/R_S \sim 100 - 1800$) is very similar to our estimate r_c in PG 1211+143. The current steady-state model is not appropriate for treating such a time-variability in its absorption features, but it is conceivable that the observed variable nature may be associated with the change in wind density (perhaps resulted from the change in mass-loading) and/or changing streamline configurations due to the variable magnetic fields. The model is in a good agreement with the data while there appears to be additional weak (intrinsic) absorbers at higher energies ($\sim 8 - 9$ keV). These weak absorption structures can be due to the resonance series converging to the Fe XXV edge (e.g. Kallman et al. 2004; Tombesi et al. 2011a). There can be also some contamination due to the presence of the background (instrumental) emission lines such as Cu K α at 8 keV in the

EPIC-pn spectrum.

In this paper we employ a well-studied semi-analytic wind model as a primary component. We feel that despite their simplicity, such models should not be dismissed off hand compared to large scale purely numerical simulations for a number of reasons: First, even the state-of-the-art simulations today have not yet provided the practical and direct observables addressed in this paper at an observationally-relevant level. Second, it is still computationally extremely challenging to include self-consistently multi-scale, multi-dimensional radiative transfer for plasma/atomic physics necessary to simulate the kind of transitions seen in UV/X-ray data while simultaneously covering a large spatial scale (say, ranging from 10 Schwarzschild radii all the way out to pc-scale) without suffering from numerical instability and boundary conditions susceptibility. In the next step a more self-consistent disk-wind morphology needs to be considered by constructing a sophisticated (perhaps dynamical) model (e.g. Ohsuga et al. 2009; Ohsuga & Mineshige 2011) also incorporating detailed radiative transfer for spectral lines (e.g. Kallman et al. 2004; Garcia et al. 2013).

In this preliminary calculation we assumed $\dot{m}_{a,o} = 1$ corresponding to the density of matter on the disk surface $n_o = 5 \times 10^{11} \text{ cm}^{-3}$. We have used slightly different values for n_o and noted their weak influence of the end results. We note that our assumed value is slightly higher than a fiducial AGN value of 10^{10} cm^{-3} (e.g. Crenshaw et al. 2003; Tombesi et al. 2011a; Gofford et al. 2013, and references therein) but its possible range can be considered as broad as $10^{10} \lesssim n_o \lesssim 10^{17} \text{ cm}^{-3}$ (e.g. Laor & Netzer 1989; George & Fabian 1991; Garcia et al. 2013) and an accurate assessment requires a more realistic modeling of accretion disk physics and its response to photoionization process.

The present analysis is based on a selected fiducial wind structure that we have examined in our earlier work (F14). Within the three-parameter model spanned by θ , kT_{bbb} and R_t in this paper, we do not notice degeneracy in the best-fit spectrum. Considering a complexity of magnetized disk-wind physics, however, it is conceivable that we may find another best-fit solution from slightly different wind conditions. Removing such potential degeneracy is in principle challenging since there is little *a priori* knowledge (at least observationally) of the underlying wind structure. Nonetheless, it will be possible to rule out some of the degenerate wind solutions by further including multiple ions of different charge states both at soft X-ray transitions (below 3-4 keV) and Fe-K α transitions simultaneously since all these absorption signatures should be coupled in the context of our continuous disk-wind scenario. We thus plan to extend the current preliminary model to include the soft X-ray WAs to examine a coherent predictability of the model using those AGNs exhibiting both WAs and UFOs.

We anticipate the upcoming missions such as *Astro-H* and *Athena* to contribute significantly to this goal by providing more detail on the Fe-K component of the wind as

well as soft X-ray absorbers, and thus to further clarify our picture of AGN structure.

We are grateful to the anonymous referee for the constructive criticism to improve the quality of the manuscript.

Table 3. Various Characteristic Radii in This Model

Symbol	Description
R_o	The fiducial radius of the wind models
R_S	Schwarzschild radius
R_t	Disk inner truncation radius
r_c	Radius where a given ion becomes most opaque
R_{ISCO}	Innermost Stable Circular Orbit

All radii are defined in the cylindrical coordinates except for r_c which is measured along a LoS direction.

REFERENCES

- Bachev, R.; Grupe, D.; Boeva, S.; Ovcharov, E.; Valcheva, A.; Semkov, E.; Georgiev, Ts.; Gallo, L. C. 2009, MNRAS, 399, 750
- Begelman, M. C., McKee, C. F., & Shields, G. A. 1983, ApJ, 271, 70
- Behar, E. et al. 2003, ApJ, 598, 232
- Behar, E., 2009, ApJ, 703, 1346
- Bentz M. C., Peterson B. M., Pogge R. W., & Vestergaard M., 2009, ApJ, 694, L166
- Blandford, R. D & Payne, D. G. 1982, MNRAS, 199, 883
- Blustin, A. J., Page, M. J., Fuerst, S. V., Branduardi-Raymont, G., & Ashton, C. E. 2005, A&A, 431, 111
- Chartas, G., Brandt, W. N., Gallagher, S. C., & Garmire, G. P. 2002, ApJ, 579, 169
- Chartas, G., Brandt, W. N., Gallagher, S. C. 2003, ApJ, 595, 85
- Chartas, G., Eracleous, M., Dai, X., Agol, E., & Gallagher, S. C. 2007, ApJ, 661, 678
- Chartas, G., Saez, C., Brandt, W. N., Giustini, M., & Garmire, G. P. 2009, ApJ, 706, 644
- Contopoulos, J., & Lovelace, R. V. E. 1994, ApJ, 429, 139 (CL94)
- Crenshaw, D. M. et al. 1999, ApJ, 516, 750
- Crenshaw, D. M., Kraemer, S. B., George, I. M. 2003, Annu. Rev. Astro. Astrophys., 41, 117
- Crenshaw, D. M. & Kraemer, S. B. 2007, ApJ, 659, 250
- Crenshaw, D. M. & Kraemer, S. B. 2012, ApJ, 753, 75
- Detmers, R. G., Kaastra, J. S., Steenbrugge, K. C., Ebrero, J., Kriss, G. A., Arav, N., Behar, E., Costantini, E., Branduardi-Raymont, G., Mehdipour, M., Bianchi, S., Cappi, M., Petrucci, P., Ponti, G., Pinto, C., Ratti, E. M., & Holczer, T. 2011, A&A, 534, 38
- Everett, J. E. 2005, ApJ, 631, 689
- Fendt, C. 2006, ApJ, 651, 272
- Ferreira, J. 1997, A&A, 319, 340

- Fukumura, K., Kazanas, D., Contopoulos, I., & Behar, E. 2010a, *ApJ*, 715, 636 (FKCB10a)
- Fukumura, K., Kazanas, D., Contopoulos, I., & Behar, E. 2010b, *ApJ*, 723, L228 (FKCB10b)
- Fukumura, K., Tombesi, F., Kazanas, D., Shrader, C., Behar, E., & Contopoulos, I. 2014, *ApJ*, 780, 120 (F14)
- Gallo, L. C.; Fabian, A. C., 2013, *MNRAS*, 434, 66
- Garcia, J., Dauser, T., Reynolds, C. S., Kallman, T. R., McClintock, J. E., Wilms, J., Eikmann, W. 2013, *ApJ*, 768, 146
- George, I. M.; Fabian, A. C. 1991, *MNRAS*, 249, 352
- George, I. M., Turner, T. J., Netzer, H., Nandra, K., Mushotzky, R. F., & Yaqoob, T. 1998, *ApJS*, 114, 73
- Giustini, M. & Proga, D. 2012, *ApJ*, 758, 70
- Gofford, J., Reeves, J. N., Tombesi, F., Baito, V., Turner, T. J., Miller, L., & Cappi, M. 2013, *MNRAS*, 430, 60
- Gofford, J.; Reeves, J. N., Baito, V., Nardini, E., Costa, M. T., Matzeu, G. A., O’Brien, P., Ward, M., Turner, T. J., & Miller, L. 2014, *ApJ*, 784, 77
- Hagino, K., Odaka, H., Done, C., Gandhi, P., Watanabe, S., Sako, M., & Takahashi, T. 2015, *MNRAS*, 446, 663
- Hanke, M., et al. 2009, *ApJ*, 690, 330
- Holczer, T., Behar, E., & Kaspi, S. 2007, *ApJ*, 663, 799
- Holczer, T. & Behar, E. 2012, *ApJ*, 747, 71
- Higginbottom, N., Proga, D., Knigge, C., Long, K. S., Matthews, J. H., & Sim, S. A. 2014, *ApJ*, 789, 19
- Kallman, T., & Bautista, M. 2001, *ApJS*, 133, 221
- Kallman, T. R., Palmeri, P., Bautista, M. A., Mendoza, C., & Krolik, J. H. 2004, *ApJS*, 155, 675
- Kazanas, D., Fukumura, K., Behar, E., Contopoulos, I., & Shrader, C. 2012, *Astronomical Review*, 7, 92
- Königl, A. & Kartje, J. F. 1994, *ApJ*, 434, 446

- Kaspi S., Smith P. S., Netzer H., Maoz D., Jannuzi B. T., & Givon U., 2000, *ApJ*, 533, 631
- Kaspi, S. & Behar, E. 2006, *ApJ*, 636, 674
- King, A. L. et al. 2012, *ApJ*, 746, 20
- King, A. L. et al. 2014, *ApJ*, 784, L2
- Kotani, T., et al. 2000, *ApJ*, 539, 413
- Kraemer, S. B., et al. 2005, *ApJ*, 633, 693
- Laor, A. & Netzer, H. 1989, *MNRAS*, 238, 897
- Luketic, S., Proga, D., Kallman, T. R., Raymond, J. C., & Miller, J. M. 2010, *ApJ*, 719, 515
- Marziani, P., Sulentic, J. W., Dultzin-Hacyan, D., Calvani, M., & Moles, M. 1996, *ApJS*, 104, 37
- Mihalas, D. 1978, *Stellar Atmospheres* (2nd ed.; New York: W. H. Freeman & Company)
- Miller, J. M., et al. 2006, *Nature*, 441, 953
- Miller, J. M., Raymond, J., Reynolds, C. S., Fabian, A. C., Kallman, T. R., & Homan, J. 2008, *ApJ*, 680, 1359
- Misawa, T., Inada, N., Oguri, M., Gandhi, P., Horiuchi, T., Koyamada, S., & Okamoto, R. 2014, *ApJ*, 794, L20
- Murphy E. M., Lockman F. J., Laor A., & Elvis M., 1996, *ApJS*, 105, 369
- Murphy, G. C., Ferreira, J., & Zanni, C. 2010, *A&A*, 512, 82
- Nardini et al. 2015, *Science*, 347, 860
- Nomura, M., Ohsuga, K., Wada, K., Susa, H., & Misawa, T. 2013, *PASJ*, 65, 40
- Ohsuga, K., Mineshige, S., Mori, M., & Kato, Y. 2009, *PASJ*, 61, L7 T. 2003, *MNRAS*, 346, 1025
- Ohsuga, K. & Mineshige, S. 2011, *ApJ*, 736, 2
- Patrick, A. R., Reeves, J. N., Porquet, D., Markowitz, A. G., Braitto, V., & Lobban, A. P. 2012, *MNRAS*, 426, 2522
- Peterson, B. M. et al. 2004, *ApJ*, 613, 682
- Porth, O. & Fendt, C. 2010, *ApJ*, 709, 1100

- Pounds, K. A. et al. 2003, MNRAS, 345, 705
- Pounds, K. A., & Page, K. L. 2006, MNRAS, 372, 1275
- Pounds, K. A. & Reeves, J. N. 2007, MNRAS, 374, 823
- Pounds, K. A. & Reeves, J. N. 2009, MNRAS, 397, 249
- Pounds, K. A. 2014, MNRAS, 437, 3221
- Proga, D., Stone, J. M., & Kallman, T. R. 2000, ApJ, 543, 686
- Proga, D. 2003, ApJ, 585, 406
- Proga, D. & Kallman, T. R. 2004, ApJ, 616, 688
- Pudritz, R. E., Rogers, C. S., & Ouyed, R. 2006, MNRAS, 365, 1131
- Reynolds, C. S., & Fabian, A. C. 1995, MNRAS, 273, 1167
- Reynolds, C. S., Ward, M. J., Fabian, A. C., & Celotti, A. 1997, MNRAS, 291, 403
- Reeves, J. N., O’Brien, P. T., & Ward, M. J. 2003, ApJ, 593, L65
- Reeves, J., Done, C., Pounds, K., Terashima, Y., Hayashida, K., Anabuki, N., Uchino, M., & Turner, M. 2008, 385, L108
- Reeves, J. N. et al. 2009, ApJ, 701, 493
- Sim, S. A. 2005, MNRAS, 356, 531
- Sim, S. A., Long, K. S., Miller, L., & Turner, T. J. 2008, MNRAS, 388, 611
- Sim, S. A., Proga, D., Miller, L., Long, K. S., & Turner, T. J. 2010, MNRAS, 408, 1396
- Steenbrugge, K. C., Kaastra, J. S., Crenshaw, D. M., Kraemer, S. B., Arav, N., George, I. M., Liedahl, D. A., van der Meer, R. L. J., Paerels, F. B. S., Turner, T. J., & Yaqoob, T., 2005, A&A, 434, 569
- Stute, M., Gracia, J., Vlahakis, N., Tsinganos, K., Mignone, A., Massaglia, S. 2014, MNRAS, 439, 3641
- Stepanovs D. & Fendt, C. 2014, arXiv:1407.3136
- Tatum, M. M., Turner, T. J., Sim, S. A., Miller, L., Reeves, J. N., Patrick, A. R., & Long, K. S. 2012, ApJ, 752, 94

- Tombesi, F., Cappi, M., Reeves, J. N., Palumbo, G. G. C., Yaqoob, T., Braitto, V., Dadina, M. 2010a, *A&A*, 521, 57
- Tombesi, F., Sambruna, R. M., Reeves, J. N., et al. 2010b, *ApJ*, 719, 700
- Tombesi, F., Cappi, M., Reeves, J. N., Palumbo, G. G. C., Braitto, V., Dadina, M. 2011a, *ApJ*, 742, 44
- Tombesi, F., Sambruna, R. M., Reeves, J. N., Reynolds, C. S., Braitto, V. 2011b, *MNRAS*, 418, L89
- Tombesi, F., Cappi, M., Reeves, J. N., & Braitto, V. 2012a, *MNRAS*, 422, L1
- Zoghbi, A. et al. *ApJ*, 799, L24